A&A, 697, A182 (2025)
https://doi.org/10.1051/0004-6361/202453641

Astronomy & Astrophysics

X-ray polarization observations of NGC 2110 with IXPE

I. Pal[1,⋆], S. Marchesi[1,2,3], N. Torres-Albà[1,4], I. Cox[1], M. Ajello[1], A. Banerjee[1], R. Silver[5], A. Pizzetti[1,6,⋆⋆], and K. Imam[1]

[1] Department of Physics and Astronomy, Clemson University, Kinard Lab of Physics, Clemson, SC 29634, USA
[2] Dipartimento di Fisica e Astronomia (DIFA), Università di Bologna, via Gobetti 93/2, I-40129 Bologna, Italy
[3] INAF – Osservatorio di Astrofisica e Scienza dello Spazio di Bologna, Via Piero Gobetti, 93/3, 40129 Bologna, Italy
[4] Department of Astronomy, University of Virginia, P.O. Box 400325, Charlottesville, VA 22904, USA
[5] NASA Goddard Space Flight Center, Greenbelt, MD 20771, USA
[6] European Southern Observatory, Alonso de Córdova 3107, Casilla 19, Santiago 19001, Chile

Received 31 December 2024 / Accepted 29 March 2025

ABSTRACT

Context. X-ray polarimetric observations from the Imaging X-ray Polarimeter Explorer (IXPE) is an excellent tool for probing the geometry and dynamics of X-ray emitting corona in active galactic nuclei (AGNs).
Aims. This work aims to investigate the geometry of the X-ray corona in the Seyfert 2 AGN, NGC 2110, using its first polarimetric observation with IXPE, conducted over a net exposure of 554 ks beginning on October 16, 2024.
Methods. We performed a model-independent analysis of the 2–8 keV IXPE polarimetric observation to estimate the polarization properties of NGC 2110. Furthermore, we performed spectral and spectro-polarimetric analyses combining IXPE data with archival observations from NuSTAR, XMM-Newton, and Swift-XRT to derive detailed spectral and polarization properties.
Results. From the spectro-polarimetric analyses, an upper limit on the polarization degree (Π_X) of 7.6% (at the 99% confidence) was estimated in the 2–8 keV band. The spectro-polarimetric analysis in the 5.66–8 keV band yielded a looser upper limit of $\lesssim$27% at the 99% confidence. This result aligns closely with the findings from the model-independent analysis.
Conclusions. Comparing the measured polarization properties, coronal parameters, and inclination angle of NGC 2110 with the Monte Carlo radiative transfer (MONK) simulations suggest that the current polarization measurements lack the sensitivity to place definitive constraints on the coronal geometry. The upper limits on Π_X, as derived from our analysis at the 99% confidence level, indicate that polarization remains undetected at a statistically significant level. Consequently, we are unable to determine whether the corona is elongated along the disk or more compact and spherical. Future observations with improved sensitivity will be crucial to breaking these degeneracies and providing deeper insight into the coronal structure of NGC 2110.

Key words. galaxies: active – galaxies: nuclei – galaxies: Seyfert – X-rays: galaxies

1. Introduction

Active galactic nuclei (AGNs), among the most luminous objects in the Universe, are powered by the accretion of matter onto the super-massive black holes (SMBHs) at the center of galaxies (Salpeter 1964; Lynden-Bell 1969; Shakura & Sunyaev 1973; Guilbert et al. 1983; Rees 1984; Ho 2008). AGNs emit across the entire electromagnetic spectrum and are widely recognized for the intense X-ray emission (Elvis et al. 1978; Mushotzky et al. 1993). The primary X-ray emission in Seyfert type AGNs is believed to originate from inverse Compton scattering of the optical-UV seed photons by the hot plasma ($\sim 10^{8-9}$ K), commonly known as corona situated near the accretion disk (Thorne & Price 1975; Sunyaev & Titarchuk 1980; Haardt & Maraschi 1991; Zdziarski et al. 2000; Done et al. 2007). Recent studies, most notably using observations from the Nuclear Spectroscopic Telescope Array (NuSTAR, Harrison et al. 2013), were able to characterize the properties of the corona in radio-quiet AGNs (e.g., its temperature, optical depth, etc., Tortosa et al. 2018; Molina et al. 2019; Baloković et al. 2020; Kamraj et al. 2022). However, despite numerous studies in the literature aimed at characterizing the corona, its geometry remains poorly understood, potentially holding vital clues to its physical origin. The launch of IXPE (Weisskopf et al. 2022) has enabled the revolutionary studies of the X-ray polarization from radio-quiet AGN coronae for the very first time, since X-ray polarimetry can independently probe coronal properties and the geometry of the corona (Marinucci et al. 2022; Tagliacozzo et al. 2023; Pal et al. 2023; Ingram et al. 2023; Gianolli et al. 2023, 2024).

Over the years, several morphological models have been proposed for the X-ray emitting corona. At least four distinct configurations have been widely suggested to describe the corona in AGNs: (1) slab (Haardt & Maraschi 1991; Beloborodov 2017), (2) wedge-shaped (Esin et al. 1997; Poutanen & Svensson 1996; Yuan & Narayan 2014; Poutanen et al. 2018; Ursini et al. 2020), (3) spherical lamppost (Matt et al. 1991; Wilkins & Fabian 2012; Ursini et al. 2021), and (4) conical outflow (Henri & Petrucci 1997; Ghisellini et al. 2004; Ursini et al. 2021). The launch of IXPE enables us to measure the polarimetric properties of radio-quiet AGNs, opening a unique window to place constraints on these proposed models. These configurations have different polarization signatures. In the slab corona model, the hot medium is uniformly distributed above the cold accretion disk, originating from magnetic instabilities. The slab corona can generate a Π_X of up to 14%, with

⋆ Corresponding author: ipal@clemson.edu
⋆⋆ ESO Fellow.

the polarization angle (Ψ_X) parallel to the accretion disk axis (Poutanen & Svensson 1996; Ursini et al. 2021; Gianolli et al. 2023). The wedge-shaped hot accretion flow resembles the slab corona with a height that increases with radius. In this scenario, the standard accretion disk is truncated at a certain radius, and the corona represents a hot accretion flow, possibly extending down to the innermost stable circular orbit (ISCO). This configuration is expected to produce an intermediate Π_X (up to 5%, depending on the inner, outer radius and the opening angle), with Ψ_X parallel to the accretion disk axis (Tagliacozzo et al. 2023). Thus, when comparing the slab and wedge-shaped coronae, the former produces a higher Π_X, while the latter results in an intermediate Π_X. In both cases, Ψ_X remains parallel to the accretion disk.

The spherical lamppost model features an isotropic spherical structure located along the spin axis of the supermassive black hole. This structure is predicted to generate a low Π_X (0–2%) with Ψ_X perpendicular to the accretion disk axis (Ursini et al. 2021). Finally, the conical outflow model is often linked to an aborted jet scenario. This configuration is expected to produce a slightly higher Π_X (up to 6%), with the Ψ_X also perpendicular to the accretion disk axis (Ursini et al. 2021). Therefore, when combined with Π_X, Ψ_X can help us break the degeneracy between different coronal geometries. The simulations using the MONK code (Zhang et al. 2019), Ursini et al. (2021) demonstrated that the Π_X for a given geometry can vary with the spectral shape, coronal temperature, optical depth, the inclination of the system and the black-hole spin. However, for spherical and conical geometries, Π_X is always significantly lower than for the slab geometry, with a 90° difference in Ψ_X between the slab/wedge and the spherical lamppost/conical outflowing coronae.

NGC 2110 is a nearby Seyfert galaxy at a redshift of $z = 0.007849$. It has a black hole mass of $\sim 2 \times 10^8\,M_\odot$ (Moran et al. 2007). NGC 2110 is an early-type spiral galaxy (SAB0) with a Seyfert 2 nucleus, located in an S0/E host galaxy at a distance of 30.4 Mpc (Wilson et al. 1985; McClintock et al. 1979). The galaxy is observed at an intermediate inclination angle, estimated between 42° and 65° (Wilson & Baldwin 1985; González Delgado et al. 2002; Kawamuro et al. 2020). Initially classified as a narrow-line X-ray galaxy, NGC 2110 has a dusty nucleus that obscures the broad-line region, leading to its Seyfert 2 optical spectrum. However, the gas column density is insufficient to attenuate the 2–10 keV emission, resulting in hard X-ray luminosities comparable to Seyfert 1 galaxies (Malaguti et al. 1999). NGC 2110 is a low-accreting AGN with an Eddington luminosity ($L_{\rm Edd}$) $= 2.4 \times 10^{46}\,{\rm erg\,s^{-1}}$ and the bolometric luminosity ranges between ($L_{\rm bol}$) $= 0.6\text{–}9 \times 10^{44}\,{\rm erg\,s^{-1}}$ (Marinucci et al. 2015). One notable characteristic of NGC 2110 is the lack of the reprocessed emission from distant Compton-thick scattering (Malaguti et al. 1999; Rivers et al. 2014; Marinucci et al. 2015). The strong iron emission lines observed in the source are believed to originate from Compton-thin material, as the lack of a significant Compton reflection component ($R \lesssim 0.2$) above 10 keV suggests the reprocessing material is not Compton-thick (Matt et al. 1991; George & Fabian 1991), makes NGC 2110 an excellent candidate for studying coronal geometry through X-ray polarization observations in the 2–8 keV band, where coronal emission dominates. In this work, we present our results on the analysis of the X-ray polarimetric observations carried out on NGC 2110 by IXPE. The observations and data reduction are described in Section 2, the analysis and results are described in Section 3, followed by the summary in Section 4.

Table 1. Observation logs of IXPE, NuSTAR, XMM-Newton & Swift observations of NGC 2110.

Telescope	OBSID	Date	Exposure Time [ks]
IXPE	03008799	2024-10-16	554
NuSTAR	60061061002	2012-10-05	16
	60061061004	2013-02-14	12
XMM-Newton	0145670101	2003-03-05	60
Swift-XRT	35459002	2006-04-08	8.6
	35459004	2008-08-31	2.2
	35459005	2009-10-12	3.0
	80364001	2012-10-05	6.5
	35459006	2013-02-03	13.0
	92804007	2017-10-13	4.5
	35459014	2019-08-07	3.3
	35459031	2020-04-08	3.7

2. Observations and data reduction

Over the past few years, NGC 2110 has been observed by several X-ray observatories. In our study, we used archival data from IXPE, NuSTAR, XMM-Newton, and Swift-XRT. The log of these observations is provided in Table 1. The data reduction process is detailed in the following subsections.

2.1. IXPE

IXPE started observing NGC 2110 on October 16, 2024, with its three detector units (DUs) for a net exposure of about 554 ks. The calibrated data were produced by the standard IXPE pipeline provided by the Science Operation Center (SOC)[1]. We used the cleaned and calibrated level 2 data for the scientific analysis. The cleaned level 2 event files were first treated with the background rejection procedure described in Di Marco et al. (2023)[2]. Then they were analyzed using the IXPEOBSSIM software v30.0.0 (Baldini et al. 2022). A count map in sky coordinates was generated using the CMAP algorithm within the xpbin task. We adopted a circular region with a radius of 60″ for the extraction of the source of the three DUs and an annulus with inner and outer radii of 150″ and 300″, respectively, for the background extraction of each DU (Di Marco et al. 2023). We then used the xpselect task to generate the filtered source and background regions.

For the spectro-polarimetric analysis, the I, Q, U source and background spectra were generated using the PHA1, PHA1Q and PHA1U algorithm using xpbin task within IXPEOBSSIM for the three DUs. The I, Q, U spectra are rebinned using ftgrouppha task, where I spectra are binned with a minimum of 30 counts/bin, and Stokes spectra are subsequently binned using I spectrum as a template file.

2.2. NuSTAR

NGC 2110 has been observed twice by NuSTAR in 2012 and 2013. Both observations are publicly available and analyzed in this work. We reduced the NuSTAR data in the 3–79 keV band using the standard NuSTAR data reduction software

[1] https://heasarc.gsfc.nasa.gov/docs/ixpe/analysis/IXPE-SOC-DOC-009-UserGuide-Software.pdf
[2] https://github.com/aledimarco/IXPE-background

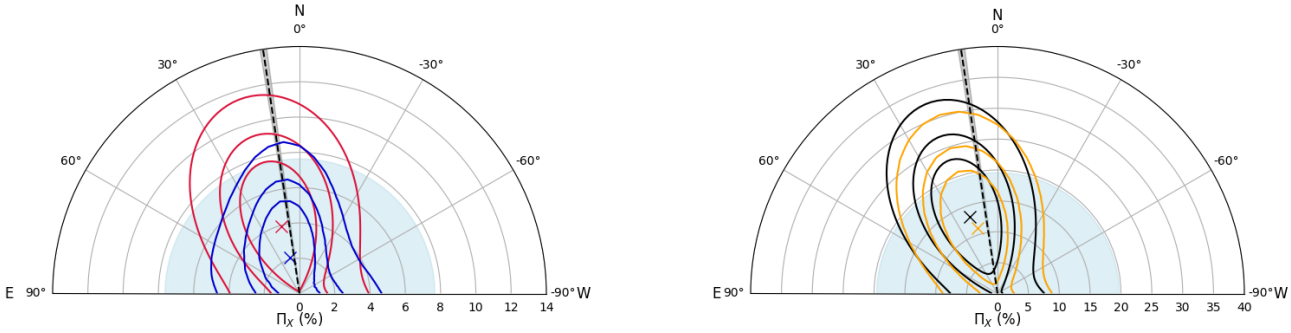

Fig. 1. Left panel: The contour plots between Π_X and Ψ_X measured in the 2–8 keV band using the PCUBE (red) and *XSPEC* (blue) analyses. The red and blue crosses are the best-fitted values of Π_X and Ψ_X. The contours are plotted in 68% (χ^2 = 2.28), 90% (χ^2 = 4.605) and 99% (χ^2 = 9.21) confidence levels. Right panel: The polarization degree Π_X and polarization angle Ψ_X contour plots as obtained from the 5.66–8 keV PCUBE (black) and *XSPEC* (orange) analyses. The black and orange crosses are the best-fitted values of Π_X and Ψ_X. The contours are plotted in 68% (χ^2 = 2.28), 90% (χ^2 = 4.605) and 99% (χ^2 = 9.21) confidence. The black dashed line represents the radio jet position angle (~8.5°) of NGC 2110. The black shaded region is the error in jet position angle. The blue shaded regions denote the MDP_{99} value at the 99% confidence.

NuSTARDAS[3] v2.1.2 distributed by HEASARC within HEASoft v6.33. The calibrated, cleaned, and screened event files were generated by running nupipeline task using the CALDB release 20220510. To extract the source counts we chose a circular region of radius 100″ centred on the source. Similarly, to extract the background counts, we selected a circular region of the same radius away from the source on the same chip to avoid contamination from source photons. We then used the nuproducts task to generate energy spectra, response matrix files (RMFs) and auxiliary response files (ARFs), for both the hard X-ray detectors housed inside the corresponding focal plane modules, FPMA and FPMB.

2.3. XMM-Newton

XMM-Newton observed NGC 2110 once in 2003 with the EPIC CCD cameras: the pn (Strüder et al. 2001) and the two MOS (Turner et al. 2001). We carried out our analysis with the data from the pn camera. We used SAS v1.3 for the data reduction. The event files were filtered to exclude background flares selected from time ranges where the 10–15 keV count rates in the PN camera exceeded 0.7 c/s. Source spectra were extracted from a circular region with a radius of 50″ centred on the nucleus. Background photons were selected from a source-free region of equal area on the same chip as the source. We checked for pileup using the EPATPLOT task. We did not find the source suffered from the pileup. We constructed RMFs and ARFs using the tasks RMFGEN and ARFGEN for each observation. Data from NuSTAR and XMM-Newton are binned with 30 counts/bin to incorporate χ^2 statistics during fitting.

2.4. Swift-XRT

There are 42 Swift/XRT observations of NGC 2110, from 2006 to 2020. To check for spectral variation over years, we have selected the observation from each year with maximum exposure (see Table 1). The corresponding spectrum was generated in the 0.5–9 keV energy band using the standard online tools provided by the UK Swift Science Data Centre (Evans et al. 2009).

The uncertainties in the spectral parameters derived from the XSPEC analysis correspond to a confidence level 90% ($\Delta\chi^2$ = 2.706), unless otherwise stated. The errors associated with the polarization parameters (Π_X and Ψ_X) obtained from the polarimetric and spectro-polarimetric analyses are quoted at a 68% confidence level, while the upper limits on the MDP and polarization parameters are reported at a 99% confidence level.

[3] https://heasarc.gsfc.nasa.gov/docs/nustar/analysis/nustarswguide.pdf

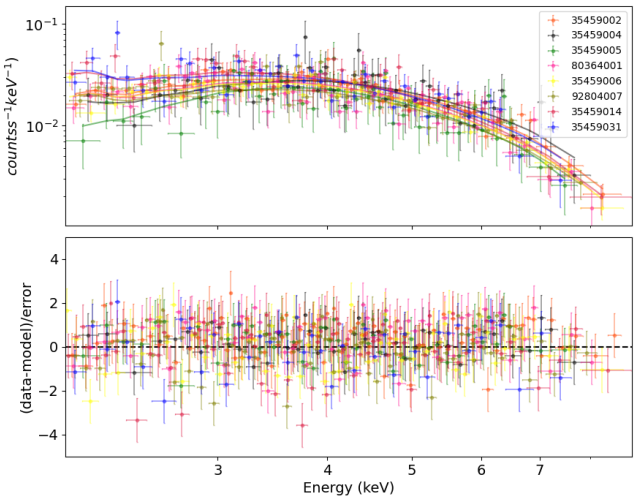

Fig. 2. Swift-XRT best-fitted spectra (top panel) with *phabs* ∗ *zphabs* ∗ (*zpo*) and the residuals (bottom panel) in the 2–9 keV band showing no significant spectral variation over years of observations.

3. Data analysis

In the following subsections, we demonstrate polarimetric and spectropolarimetric analyses of the IXPE, NuSTAR, XMM-Newton, and Swift-XRT observations.

3.1. Polarimetry

The polarimetric signal of NGC 2110 was analyzed in a model-independent way using the PCUBE algorithm based on Kislat et al. (2015) method in the xpbin task with the software ixpeobssim v30.0.0 (Baldini et al. 2022). The three polarization cubes for the three DUs were generated to extract information such as Stokes parameters; MDP_{99}; Π_X; Ψ_X and their associated errors. We first generated the three polarization cubes corresponding to the three DUs across the entire 2–8 keV energy

Table 2. Polarization parameters in different energy bands as obtained from PCUBE analysis.

Energy	$\Pi_X \pm \delta\Pi_X$ [%]	$\Psi_X \pm \delta\Psi_X$ [deg.]	MDP_{99} [%]	$\Pi_{X_{99}}$ [%]
2–8	3.93 ± 2.52	15 ± 18	7.65	<10.48
2–4	2.11 ± 2.38	-23 ± 32	8.03	<8.30
4–8	7.19 ± 3.75	22 ± 15	11.39	<16.94
2–2.83	1.13 ± 4.26	-69 ± 108	11.92	<12.21
2.83–4	3.77 ± 2.88	-17 ± 22	8.72	<11.26
4–5.66	1.87 ± 3.50	38 ± 54	10.61	<10.97
5.66–8	13.18 ± 6.47	20 ± 14	19.64	<30.00

Notes. The errors in Π_X and Ψ_X are quoted at the 68% confidence. MDP_{99} quantifies the polarization sensitivity at the 99% confidence level. The upper limits at the 99% confidence level for one parameter of interest ($\Pi_{X_{99}}$) are also reported.

Table 3. Parameters obtained from the best-fitted model *phabs* ∗ *zphabs* ∗ (*zpo*) to the XRT observations of NGC 2110.

OBSID	$N_{H,los}$ [$\times 10^{22}$ cm^{-2}]	Γ	norm	c_{stat}/d.o.f.
35459002	$3.63^{+1.37}_{-1.33}$	$1.38^{+0.36}_{-0.35}$	$0.02^{+0.02}_{-0.01}$	152/167
35459004	<6.45	<1.44	<0.02	27/42
35459005	$6.15^{+3.15}_{-2.91}$	$1.56^{+0.79}_{-0.75}$	<0.15	35/50
80364001	$3.27^{+1.67}_{-1.60}$	$1.21^{+0.45}_{-0.44}$	$0.03^{+0.04}_{-0.02}$	115/116
35459006	$2.98^{+1.15}_{-1.12}$	$1.14^{+0.31}_{-0.30}$	$0.03^{+0.02}_{-0.01}$	221/209
92804007	$2.57^{+1.99}_{-1.91}$	$1.09^{+0.54}_{-0.52}$	$0.006^{+0.010}_{-0.004}$	81/87
35459014	$2.39^{+1.92}_{-1.84}$	$1.32^{+0.54}_{-0.53}$	$0.007^{+0.011}_{-0.004}$	94/77
35459031	<4.82	$1.05^{+0.58}_{-0.47}$	$0.005^{+0.008}_{-0.003}$	89/79

band. The combined polarization parameters are presented in Table 2. From the PCUBE analysis, we obtained $\Pi_X = 3.93\% \pm 2.52\%$ at the 68% confidence level, with an upper limit of $\lesssim$10.48% at 99% confidence. The contours of Π_X versus Ψ_X at the 68% ($\chi^2 = 2.28$), 90% ($\chi^2 = 4.605$), and 99% ($\chi^2 = 9.21$) confidence levels are shown in the left panel of Fig. 1.

To investigate the energy dependence of the polarization parameters, we derived these parameters in multiple energy bins using the PCUBE algorithm. The 2–8 keV range was divided into 2–12 bins (e.g., for two bins: 2–4 keV and 4–8 keV). Table 2 presents the polarization parameters for the 2–8 keV data, divided into two and four energy bins. The largest Π_X value was measured in the 5.66–8 keV band, where we obtained $\Pi_X = 13.18\% \pm 6.47\%$ at the 68% confidence. Contour plots of Π_X versus Ψ_X were generated to evaluate the detection significance in this band (see right panel of Fig. 1). We obtained an upper limit of 30% for Π_X. However, considering the entire 2–8 keV band or dividing it into multiple bins, no significant polarization detection can be claimed in any energy range as the measured Π_X values remain lower than the MDP values. The absence of a significant polarization degree suggests that the polarization angle remains unconstrained.

3.2. IXPE, NuSTAR, XMM-Newton and Swift-XRT spectral and spectro-polarimetric analysis

The X-ray spectra of NGC 2110 have been widely studied in the past few years (Reeves et al. 2006; Evans et al. 2007; Marinucci et al. 2015; Kawamuro et al. 2016; Baloković et al. 2020; Tanimoto et al. 2020; Kang & Wang 2022; Diaz et al. 2023; Jana et al. 2023). Previous studies indicate the presence of intense iron lines in the source spectrum. However, the spectral fitting supports the presence of a very weak Compton reflection with a reflection fraction (R) of $\lesssim$0.15 (Malaguti et al. 1999; Rivers et al. 2014; Marinucci et al. 2015; Jana et al. 2023), originating from circumnuclear material partially covered by several layers of absorbing material with column densities in the range $2\text{–}6 \times 10^{22}$ cm^{-2} (Marinucci et al. 2015). The reprocessed emission from NGC 2110 has been studied using both the reflection and the borus model; however, all models are consistent with a Compton-thin absorber in the line of sight to the primary coronal emission with $N_{H_{los}} \sim 10^{22}$ atoms cm^{-2}. Therefore, the previous analyses cumulatively suggest that NGC 2110 is one of the few Seyfert 2 sources where the strong iron lines are not produced by distant, Compton-thick material but are instead emitted by Compton-thin matter. Past analyses performed using several instruments such as, BeppoSAX, NuSTAR, XMM-Newton, Swift-XRT & Suzaku have shown that the spectra of NGC 2110 can be well fitted with an absorbed power-law continuum with photon index (Γ) ~ 1.7. This suggests that the source has not undergone any dramatic spectral shape alteration over the years of observations. However, there is evidence of a change in the intensity of the iron K lines with the flux state of the source on time scales of years (Marinucci et al. 2015). Therefore, we left the line components free to vary during the joint spectral fit. The previous studies on the broadband analysis of NGC 2110 spectra (Reeves et al. 2006; Evans et al. 2007) also reported a presence of the extra-nuclear emission in the softer-energy (E < 1 keV) part of the spectra. Since the analysis of that component is beyond the scope of this work, our analysis was limited to the E $\gtrsim$ 2 keV band.

3.2.1. Spectral analysis with an absorbed power-law

To investigate any spectral variations over the years, we performed the spectral fitting of the eight Swift-XRT observations taken between 2006 and 2020. Due to the limited signal-to-noise ratio (S/N), the 2–9 keV XRT data were binned with a minimum of 5 counts per bin, and the c-statistics were applied during the fitting process. Each XRT spectrum was fitted independently using a simple absorbed power-law model: *phabs* ∗ *zphabs* ∗ (*zpo*). In this model, *phabs* accounts for the Milky-Way hydrogen column density, which was fixed at 3.01×10^{22} atoms cm^{-2}, as adopted from Willingale et al. (2013). The best-fit parameters, presented in Table 3, indicate no significant variation in Γ or $N_{H_{los}}$ within the uncertainties, therefore, suggesting no prominent spectral evolution of NGC 2110 (see Fig. 2). We continued the absorbed power-law fitting with the 2012 and 2013 NuSTAR observations separately in an energy band that partially coincides with the IXPE band (i.e., 3–8 keV). The Fe Kα line emission in the NuSTAR spectrum was modeled with a Gaussian component. The 3–8 keV spectral analysis of the 2012 NuSTAR data with the model *constant* ∗ *phabs* ∗ *zphabs* ∗ (*zpo* + *zgauss*) yielded $\Gamma = 1.65 \pm 0.05$, $N_{H_{los}} = 3.96 \pm 0.43 \times 10^{22}$ atoms cm^{-2}, energy of the Fe Kα line ($Line_E$) = 6.26 ± 0.07 keV, the calibration constant between FPMA and FPMB ($C_{FPMA/FPMB}$) = 1.01 ± 0.01, χ^2/d.o.f. = 243/242 and 3–8 keV flux (f_{3-8}) = 1.50×10^{-10} erg cm^{-2} s^{-1}. A similar analysis of the 2013 NuSTAR data produced $\Gamma = 1.67 \pm 0.07$, $N_{H_{los}} = 5.35 \pm 0.96 \times 10^{22}$ atoms cm^{-2}, $Line_E = 6.42 \pm 0.06$ keV, $C_{FPMA/FPMB} = 1.00 \pm 0.01$, χ^2/d.o.f. =

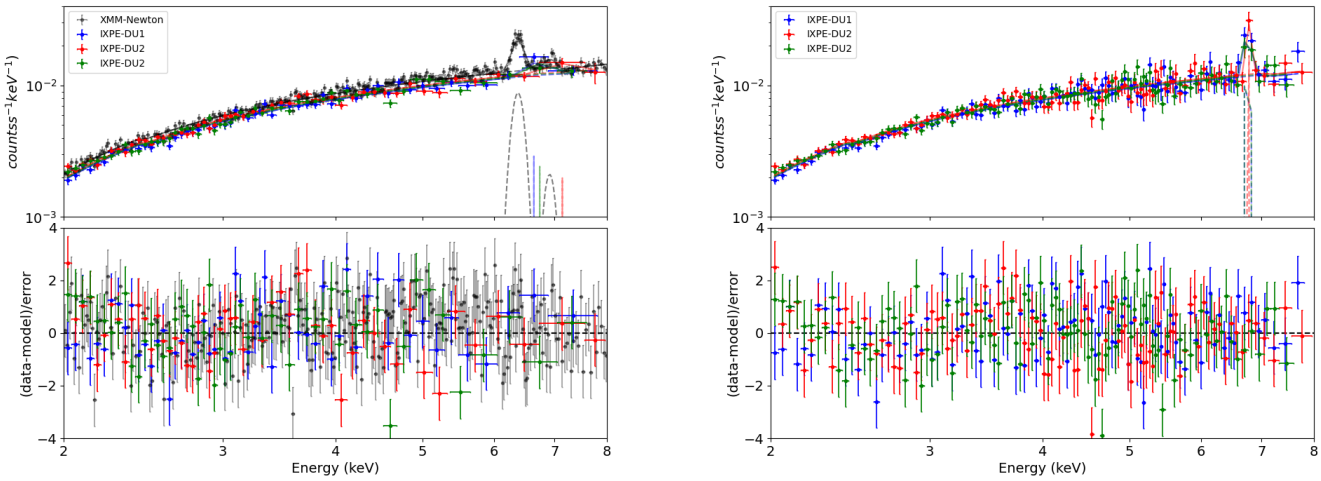

Fig. 3. Left panel: Best-fitted XMM-Newton and IXPE I-spectra and right panel: Best-fitted IXPE I-spectra with power-law model *constant* ∗ *phabs* ∗ *zphabs* ∗ (*zpo* + *zgauss*) with data to model residues.

239/242 and $f_{3-8} = 1.01 \times 10^{-10}$ erg cm^{-2} s^{-1}. The Fe Kα line widths were frozen at 100 eV for both NuSTAR observations as allowing them to vary did not improve the fit statistics. Fitting the 2–8 keV XMM-Newton PN data with the absorbed power-law model produced similar best-fit parameters. To take care of the Fe Kβ line component in XMM spectrum we had to add another *zgauss* component and thus, the new model looks like, *phabs* ∗ *zphabs*∗(*zpo*+*zgauss*+*zgauss*). The spectral parameters obtained are: $\Gamma = 1.45 \pm 0.04$, $N_{H_{los}} = 4.17 \pm 0.24 \times 10^{22}$ atoms cm^{-2}, energy of the Fe Kα line ($Line_{E1}$) = 6.42 ± 0.01 keV, line width (σ_1) = 0.05 ± 0.02 keV, energy of the Fe Kβ line ($Line_{E1}$) = $6.91^{+0.14}_{-0.21}$ keV, $\sigma_2 < 0.28$ kev, χ^2/d.o.f. = 1061/1094 and $f_{3-8} = 1.71 \times 10^{-11}$ erg cm^{-2} s^{-1}.

Next, we included the IXPE I-spectra in our analysis. Although NGC 2110 showed no significant spectral shape variations over years of observation, we detected flux variations between the 2003 XMM-Newton and the 2012–2013 NuSTAR observations in the 3–8 keV band, which partially overlaps with the IXPE range. Therefore, we fitted the IXPE data separately with the NuSTAR and XMM-Newton observations. The Fe line components for the NuSTAR and XMM-Newton observations were fixed to the best-fit values obtained earlier, and the model parameters were tied across instruments. The calibration constants between the instruments were varied. The results from the absorbed power-law fit are summarized in Table 4. The calibration constants between observations indicate that the IXPE 2024 observation ($f_{2-8} \simeq 1.74 \times 10^{-11}$ erg cm^{-2} s^{-1}) corresponds to a flux state similar to the 2003 XMM-Newton observation ($f_{2-8} = 1.97 \times 10^{-11}$ erg cm^{-2} s^{-1}), as further supported by the best-fit spectra and residuals shown in Fig. 3.

Since the spectral parameters of the joint fit with IXPE, NuSTAR, and XMM-Newton are primarily driven by the higher S/N ratio of the latter two, we also performed an independent absorbed power-law fit to the 2–8 keV IXPE I-spectra. The best-fit parameters were: $\Gamma = 1.49 \pm 0.10$, $N_{H_{los}} = 4.08 \pm 0.43 \times 10^{22}$ atoms cm^{-2}, energy of the Fe Kα line ($Line_{E1}$) = 6.81 ± 0.30 keV, χ^2/d.o.f. = 344/320 and $f_{2-8} = 1.74 \times 10^{-11}$ erg cm^{-2} s^{-1}. The width of the iron line was frozen to 10 eV.

3.2.2. Spectro-polarimetric analysis

For the spectro-polarimetric fit, we simultaneously fitted the IXPE I-spectra and Stokes spectra (IXPE Q and U-spectra) from all three DUs with an absorbed power-law (*zphabs* ∗ *zpo*) convolved with the polarization model *polconst*. A *zgauss* component was added to model the weak Fe emission line in the IXPE I-spectra. Since iron lines are expected to be unpolarized (Goosmann & Matt 2011; Marin et al. 2018), we fixed the polarization of the *zgauss* components to zero. The final model was: *constant* ∗ *phabs* ∗ *zphabs* ∗ (*polconst* ∗ *zpo* + *polconst*^{0} ∗ *zgauss*), where *polconst*^{0} represents zero polarization. The *constant* account for the calibration differences between the DUs, with DU1 fixed at 1.0, and DU2 and DU3 yielding 1.00 ± 0.13 and 0.99 ± 0.14, respectively.

From the spectro-polarimetric fit in the 2–8 keV band, we obtained $\Pi_X = 2.12 \pm 2.05\%$ and $\Psi_X = 14^{\circ}{}^{+43^{\circ}}_{-31^{\circ}}$ at the 68% confidence, with an upper limit of $\Pi_X < 7.6\%$ at the 99% confidence. The contours Π_X versus Ψ_X are shown in Fig. 1. Since the highest Π_X was measured in the 5.66–8 keV band of the algorithm PCUBE, we performed a spectropolarimetric analysis in

Table 4. Best-fitted parameters obtained using the model *constant* ∗ *phabs* ∗ *zphabs* ∗ (*zpo* + *zgauss*) to the joint IXPE and NuSTAR/XMM-Newton observations of NGC 2110.

Parameter	IXPE +NuSTAR (2012)	IXPE +NuSTAR (2013)	IXPE +XMM
$N_{H,los}$	$4.70^{+0.20}_{-0.20}$	$4.56^{+0.22}_{-0.22}$	$4.51^{+0.13}_{-0.13}$
Γ	$1.65^{+0.03}_{-0.03}$	$1.61^{+0.04}_{-0.04}$	$1.45^{+0.04}_{-0.04}$
norm	$6.2^{+0.3}_{-0.3}$	$4.0^{+0.3}_{-0.3}$	$0.51^{+0.03}_{-0.03}$
χ^2/d.o.f.	613/564	608/564	1447/1418
$C_{FPMA/FPMB}$	$1.015^{+0.009}_{-0.010}$	$1.000^{+0.014}_{-0.014}$	–
$C_{FPMA/DU1}$	$0.096^{+0.002}_{-0.002}$	$0.141^{+0.003}_{-0.003}$	–
$C_{FPMA/DU2}$	$0.100^{+0.002}_{-0.002}$	$0.147^{+0.003}_{-0.003}$	–
$C_{FPMA/DU3}$	$0.098^{+0.002}_{-0.002}$	$0.144^{+0.003}_{-0.003}$	–
$C_{XMM/DU1}$	–	–	$0.90^{+0.01}_{-0.01}$
$C_{XMM/DU2}$	–	–	$0.93^{+0.01}_{-0.01}$
$C_{XMM/DU3}$	–	–	$0.91^{+0.01}_{-0.01}$

Notes. $N_{H,los}$ and the normalizations are in units of 10^{22} atoms cm^{-2} and 10^{-2}.

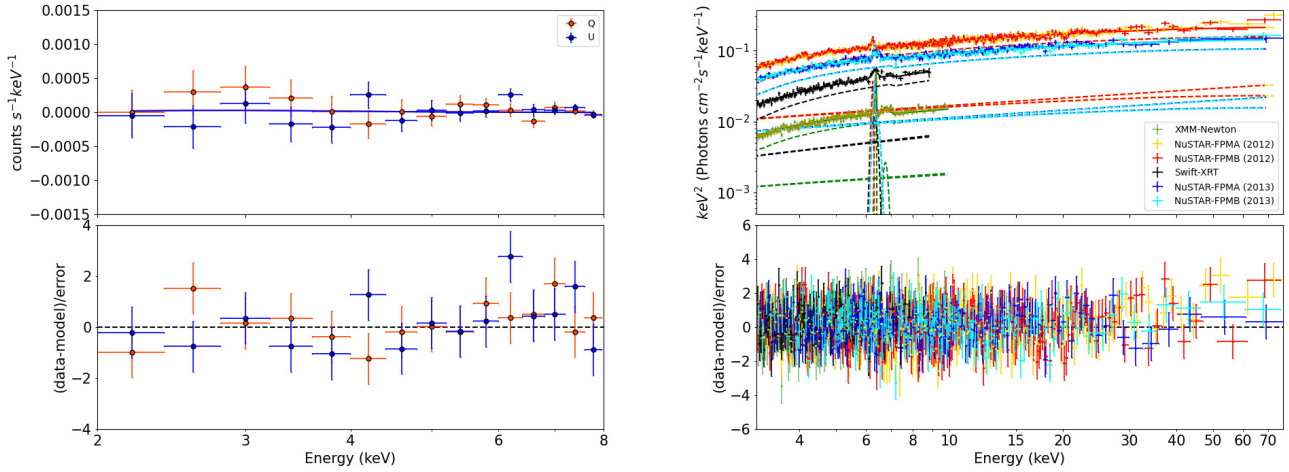

Fig. 4. Left panel: IXPE Q, U stokes best-fit data with model: *constant* ∗ *phabs* ∗ *zphabs* ∗ (*zpo* + *zgauss*) and the residuals. Right panel: NuSTAR, XMM-Newton and Swift-XRT unfolded best-fitted spectra with model: *constant* × *phabs* × (*zphabs* × *zcutoff* + *pexrav* + *zgauss*) (top panel) and the residuals (bottom panel).

this range, obtaining $\Pi_X = 11.16 \pm 6.32\%$ and $\Psi_X = 18° \pm 17°$ at 68% confidence, with an upper limit of $\Pi_X < 27\%$ at 99% confidence. The corresponding contours Π_X versus Ψ_X are also shown in Fig. 1. The best-fitted IXPE Q, U- spectra are plotted in Fig. 4.

3.2.3. Coronal properties of NGC 2110 with NuSTAR

To begin examining the coronal properties of NGC 2110, we fitted the 3–78 keV 2012 NuSTAR (OBSID – 60061061002) observation with the following model:

$$constant \times phabs \times (zphabs \times zcutoff + pexrav + zgauss). \quad (1)$$

The primary emission was modeled using an absorbed cutoff-power law, zphabs × zcutoff. For the reprocessed emission, we used the reflection model *pexrav* with a fixed inclination angle of 60° (Marinucci et al. 2015). The iron Kα emission line in the NuSTAR spectrum was modeled with a *zgauss* component. The best-fit parameters from the spectral analysis of the 2012 NuSTAR spectrum are as follows: $\Gamma = 1.69^{+0.01}_{-0.04}$, cut-off energy ($E_{cut}$) $= 484.50^{+u}_{-210.22}$ keV[4], reflection-fraction (R) < 0.13. The χ^2/dof for the fit was 1392/1407. During fitting, Γ, E_{cut} and the model normalizations were tied between *zcutoff* and *pexrav*. Next, we proceed by adding the 2013 NuSTAR observation to the best-fitted model and performed an joint analysis by leaving the model parameters and nrmalizations vary between two observations. For the newly added observation (OBSID – 60061061004), we obtained, $\Gamma = 1.70^{+0.04}_{-0.05}$, $E_{cut} = 317.67^{+u}_{-137.49}$ keV and $R < 0.15$. the line widths were frozen at 10 eV for both observations. Our analysis agrees well with the findings of Marinucci et al. (2015).

Since, the joint analysis of the two NuSTAR observations did not show any changes in the spectral properties and the source was found to be at a similar flux state, we proceed with the joint analysis by tying all the spectral parameters together. We used the physically motivated comptonization model *xillverCP* (García et al. 2014) to calculate the coronal temperature (kT_e) of the source. From the joint fit, we obtained the line-of-sight column density (N_H) $= 5.99 \pm 0.23 \times 10^{22}$ atoms cm^{-2}, $\Gamma = 1.74 \pm 0.01$ and $kT_e > 74.86$ keV. The χ^2/d.o.f. of the fit was 1414/1406. The Fe-Kα line was self-consistently taken care of by *xillverCP*. We also varied the inclination angle (i) during the spectral fit and obtained a lower limit of $i > 74°$. The upper limit of the optical depth (τ) as calculated using the following equation (Zdziarski et al. 1996; Życki et al. 1999),

$$\tau = \sqrt{\frac{9}{4} + \frac{3}{\theta\left[\left(\Gamma + \frac{1}{2}\right)^2 - \frac{9}{4}\right]}} - \frac{3}{2} \quad (2)$$

is <1.61, where $\theta = kT_e/m_e c^2$.

Next, we performed a joint analysis of the NuSTAR, XMM-Newton, and Swift-XRT observations using our best-fit model:

constant × phabs × (zphabs × *zcutoff* + pexrav + zgauss)

in the ≳3 keV band. For this joint analysis, all 42 Swift-XRT observations taken between 2006 and 2020 were combined and grouped with a minimum of 50 counts per bin.

Following Evans et al. (2007), we modeled the XMM-Newton Fe-Kα (6.42 ± 0.01 keV) and Fe-Kβ (7.01 ± 0.04 keV) lines with two different *zgauss* components with their width frozen to 10 eV. We also added a neutral Fe K edge to the model. The Swift-XRT observations were fitted together with a Fe-Kα line component. From the joint spectral analysis, we derived $N_H = (5.86^{+0.62}_{-0.61}) \times 10^{22}$ atoms cm^{-2}, $\Gamma = 1.71^{+0.01}_{-0.02}$, and $E_{cut} = 280^{+65}_{-54}$ keV. The best fit spectra with residuals are plotted in Fig. 4. Our measurements of N_H and Γ are consistent with previous results obtained from Suzaku (Rivers et al. 2014; Kawamuro et al. 2016; Tanimoto et al. 2020) as well as NuSTAR observations (Marinucci et al. 2015; Baloković et al. 2020; Jana et al. 2023). While Baloković et al. (2020) and Jana et al. (2023) reported $E_{cut} = 300^{+50}_{-30}$ keV and 218^{+35}_{-47} keV, respectively, Marinucci et al. (2015) provided a lower limit of $E_{cut} > 210$ keV.

Furthermore, fitting the Comptonization model, *constant* ∗ *phabs*∗*zphabs*∗(*xillverCP*) to the NuSTAR, XMM-Newton and XRT data allowed us to put a tighter constraint on the inclination angle compared to the NuSTAR-only fit. The best fit model parameters for the joint fit are given in Table 5.

4. Discussion and summary

Till now, IXPE polarimetric observations have been utilized to investigate the morphology of X-ray coronae in

[4] *u* in the error denotes an upper limit on the parameter.

Table 5. Spectral analysis results from the joint analysis of NuSTAR, XMM-Newton and XRT observations.

Model component	Parameter	Best-Fit
zphabs	$N_{H,los}$ ($\times 10^{22}$) cm^{-2}	$5.86^{+0.62}_{-0.61}$
pexrav	Γ	$1.71^{+0.01}_{-0.02}$
	E_{cut} (keV)	280^{+65}_{-54}
	norm ($\times 10^{-2}$)	$3.82^{+0.10}_{-0.21}$
	χ^2/d.o.f.	3805/3727
xillverCP	Γ	$1.78^{+0.01}_{-0.01}$
	kT_e	>54
	R	$0.40^{+0.07}_{-0.06}$
	norm ($\times 10^{-3}$)	$1.77^{+0.01}_{-0.01}$
	θ (°)	$86.0^{+0.5}_{-0.6}$
	χ^2/d.o.f.	3757/3736
	XMM-Newton	
zgauss	$Line_{E1}$ (keV)	$6.42^{+0.01}_{-0.01}$
	$norm_{E1}$ ($\times 10^{-5}$)	$4.55^{+0.40}_{-0.40}$
	$Line_{E2}$ (keV)	$7.01^{+0.04}_{-0.04}$
	$norm_{E2}$ ($\times 10^{-5}$)	$1.07^{+0.34}_{-0.34}$
	NuSTAR (2012)	
zgauss	$Line_{E1}$ (keV)	$6.27^{+0.08}_{-0.08}$
	$norm_{E1}$ ($\times 10^{-5}$)	$8.90^{+0.34}_{-0.34}$
	NuSTAR (2013)	
zgauss	$Line_{E1}$ (keV)	$6.41^{+0.06}_{-0.06}$
	$norm_{E1}$ ($\times 10^{-5}$)	$2.23^{+0.50}_{-0.50}$
	Swift-XRT	
zgauss	$Line_{E1}$ (keV)	$6.39^{+0.07}_{-0.06}$
	σ	<0.17
	$norm_{E1}$ ($\times 10^{-5}$)	$3.43^{+0.16}_{-0.15}$

three unobscured radio-quiet Seyfert galaxies: MCG-05-23-16 (Marinucci et al. 2022; Tagliacozzo et al. 2023), NGC 4151 (Gianolli et al. 2023, 2024), and IC 4329A (Pal et al. 2023; Ingram et al. 2023). From the first IXPE observation of MCG-05-23-16, Marinucci et al. (2022) reported an lower limit on Π_X of $\gtrsim$4.7% at the 99% confidence level. After combining the first observation with the second, Π_X of the primary continuum was found to be $\gtrsim$3.2% at the 99% confidence level (Tagliacozzo et al. 2023). Both observations suggested a hint of alignment between the polarization angle and the accretion disc spin axis, disfavoring a spherical geometry. For IC 4329A, a 3σ upper limit on Π_X of 6.2% was measured. In NGC 4151, a clear detection was reported with $\Pi_X = 4.9 \pm 1.1$%. In both IC 4329A and NGC 4151, Ψ_X was found to be parallel to the disc axis, disfavoring the spherical lamppost geometry.

In this work, we conducted polarimetric and spectro-polarimetric analyses of NGC 2110 using the first IXPE observation. A model-independent analysis of its polarization properties, performed using polarization cubes (PCUBE) across multiple energy bands, is presented in Table 2. In each energy band, the measured polarization degree remains below the MDP values, preventing us from claiming a significant polarization detection for NGC 2110. As a result, the polarization angle remains unconstrained across all energy bands. While Table 2 suggests an increase in polarization degree with energy, this trend is likely a consequence of rising upper limits due to the decreasing signal-to-noise ratio at higher energies. Our model-dependent analysis in the 2-8 keV band supports the PCUBE results, placing an upper limit of 7.6% on Π_X at the 99% confidence level. Furthermore, our analysis of the 5.66–8 keV IXPE I, Q, and U spectra, including contour plots between Π_X and Ψ_X (Fig. 1, right panel), constrains the upper limit of Π_X to <27% at the 99% confidence.

From an analysis of NGC 2110, VLA 3.6 and 20 cm observations, Nagar et al. (1999) reported a radio jet position angle (PA) of 9°. Using VLBA 8.4 GHz radio continuum observations, Mundell et al. (2000) measured a North-South radio jet PA of 8.5° ± 0.8°. However, the upper limits on Π_X obtained from both our polarimetric and spectro-polarimetric analyses of the primary emission in the 2–8 keV band prevent us from placing a meaningful constraint on Ψ_X, making it difficult to draw definitive conclusions about the coronal geometry of NGC 2110. Additionally, the contour plot between Π_X and Ψ_X does not allow us to determine whether the radio jet position angle is aligned parallel or perpendicular to Ψ_X.

The earlier analysis for MCG-05-23-16 and NGC 4151 (Marinucci et al. 2022; Tagliacozzo et al. 2023; Gianolli et al. 2023) shows that Ψ_X being parallel to the accretion disk disfavors a spherical or cone-shaped corona considering the systems inclinations $\gtrsim$40°−50°, which are typical for Seyfert galaxies. A polarization angle parallel to the accretion disk axis indicates that a flat configuration of the emitting matter is more likely to produce such a scenario. This is supported by simulations of polarization signals for various coronal geometries, including slab, cone, and spherical models (Ursini et al. 2021). Using the *MONK* (Zhang et al. 2019) code, Ursini et al. (2021) demonstrated in their simulations that Ψ_X for slab and spherical/conical coronas is not strongly dependent on energy or system inclination. There is always a 90° difference in Ψ_X between the slab and cone or spherical corona. While for the slab geometry, Ψ_X is parallel to the disk axis, for conical/spherical ones it is perpendicular to the accretion disk axis. The simulation also revealed that Π_X is influenced by coronal parameters (Γ, kT_e, τ), corona size/black-hole spin, and system inclination. At low inclination, it is challenging to distinguish between coronal geometries when $\Pi_X \sim 0$−2%. However, for high-inclination systems, distinct differences in Π_X emerge among geometries (see Fig. 2 of Ursini et al. 2021). At high inclinations, a slab corona produces polarization degrees up to 12%. Due to the symmetrical nature of a spherical corona, the expected polarization degree is significantly lower (∼1−3%) compared to a slab geometry (Poutanen & Svensson 1996; Tamborra et al. 2018). For a conical corona, the expected polarization lies between that of the slab and spherical geometries. Recently, Tagliacozzo et al. (2023) used the *MONK* code to simulate polarization signals for a wedge-shaped corona in MCG-05-23-16. They found that the wedge-shaped geometry is similar to the slab, producing Ψ_X parallel to the accretion disk axis. Moreover, the wedge-shaped configuration resolves the issue of slab geometry producing only super-soft ($\Gamma \geq 2.0$) X-ray spectra (Stern et al. 1995; Done et al. 2007; Poutanen et al. 2018).

Our broad-band spectral analysis of the NuSTAR observations of NGC 2110 using the Comptonization model, *xillverCP* yielded a photon index, Γ of 1.74 ± 0.01 and a lower limit of the electron temperature, kT_e of 74.86 keV, implying an optical depth, τ of <1.61. Additionally, we derived a lower limit on

the inclination angle, finding $i > 74°$. The joint analysis of the NuSTAR, XMM-Newton, and Swift-XRT data using the same Comptonization model produced consistent spectral parameters (see Table 5). Comparing our best-fit values of kT_e and inclination angle with the simulations from Marinucci et al. (2022) and Tagliacozzo et al. (2023) suggests that, while the high inclination of NGC 2110 makes it a promising candidate for polarization studies to probe its coronal geometry, the current polarization measurements lack the sensitivity to place definitive constraints on the polarization parameters. Contour plots from our XSPEC analysis indicate that the upper limit on Π_X (at the 99% confidence in the 2–8 keV band) is approximately 8% if the polarization is aligned with the radio jet (suggesting a corona elongated along the disk) and around 4% if perpendicular (consistent with a more spherical corona). Given these constraints, the existing data do not allow us to draw definitive conclusions about the coronal structure of NGC 2110.

Acknowledgements. We thank the referee for their valuable suggestions, which have helped improve the clarity of the paper. The IXPE data used in this paper are publicly available in the HEASARC database: https://heasarc.gsfc.nasa.gov/docs/ixpe/archive/. We thank the NuSTAR Operations, Software, and Calibration teams for their support in the execution and analysis of these observations. This research has made use of archival data from the XMM-Newton and NuSTAR observatories, accessed through the High Energy Astrophysics Science Archive Research Center (HEASARC) online service, provided by the NASA Goddard Space Flight Center.

References

Baldini, L., Bucciantini, N., Lalla, N. D., et al. 2022, SoftwareX, 19, 101194
Baloković, M., Harrison, F. A., Madejski, G., et al. 2020, ApJ, 905, 41
Beloborodov, A. M. 2017, ApJ, 850, 141
Di Marco, A., Soffitta, P., Costa, E., et al. 2023, AJ, 165, 143
Diaz, Y., Hernàndez-García, L., Arévalo, P., et al. 2023, A&A, 669, A114
Done, C., Gierliński, M., & Kubota, A. 2007, A&ARv, 15, 1
Elvis, M., Maccacaro, T., Wilson, A. S., et al. 1978, MNRAS, 183, 129
Esin, A. A., McClintock, J. E., & Narayan, R. 1997, ApJ, 489, 865
Evans, D. A., Lee, J. C., Turner, T. J., Weaver, K. A., & Marshall, H. L. 2007, ApJ, 671, 1345
Evans, P. A., Beardmore, A. P., Page, K. L., et al. 2009, MNRAS, 397, 1177
García, J., Dauser, T., Lohfink, A., et al. 2014, ApJ, 782, 76
George, I. M., & Fabian, A. C. 1991, MNRAS, 249, 352
Ghisellini, G., Haardt, F., & Matt, G. 2004, A&A, 413, 535
Gianolli, V. E., Kim, D. E., Bianchi, S., et al. 2023, MNRAS, 523, 4468
Gianolli, V. E., Bianchi, S., Kammoun, E., et al. 2024, A&A, 691, A29
González Delgado, R. M., Arribas, S., Pérez, E., & Heckman, T. 2002, ApJ, 579, 188
Goosmann, R. W., & Matt, G. 2011, MNRAS, 415, 3119
Guilbert, P. W., Fabian, A. C., & Rees, M. J. 1983, MNRAS, 205, 593
Haardt, F., & Maraschi, L. 1991, ApJ, 380, L51
Harrison, F. A., Craig, W. W., Christensen, F. E., et al. 2013, ApJ, 770, 103
Henri, G., & Petrucci, P. O. 1997, A&A, 326, 87
Ho, L. C. 2008, ARA&A, 46, 475
Ingram, A., Ewing, M., Marinucci, A., et al. 2023, MNRAS, 525, 5437
Jana, A., Chatterjee, A., Chang, H.-K., et al. 2023, MNRAS, 524, 4670
Kamraj, N., Brightman, M., Harrison, F. A., et al. 2022, ApJ, 927, 42
Kang, J.-L., & Wang, J.-X. 2022, ApJ, 929, 141
Kawamuro, T., Ueda, Y., Tazaki, F., Ricci, C., & Terashima, Y. 2016, ApJS, 225, 14
Kawamuro, T., Izumi, T., Onishi, K., et al. 2020, ApJ, 895, 135
Kislat, F., Clark, B., Beilicke, M., & Krawczynski, H. 2015, Astropart. Phys., 68, 45
Lynden-Bell, D. 1969, Nature, 223, 690
Malaguti, G., Bassani, L., Cappi, M., et al. 1999, A&A, 342, L41
Marin, F., Dovčiak, M., & Kammoun, E. S. 2018, MNRAS, 478, 950
Marinucci, A., Matt, G., Bianchi, S., et al. 2015, MNRAS, 447, 160
Marinucci, A., Muleri, F., Dovciak, M., et al. 2022, MNRAS, 516, 5907
Matt, G., Perola, G. C., & Piro, L. 1991, A&A, 247, 25
McClintock, J. E., van Paradijs, J., Remillard, R. A., et al. 1979, ApJ, 233, 809
Molina, M., Malizia, A., Bassani, L., et al. 2019, MNRAS, 484, 2735
Moran, E. C., Barth, A. J., Eracleous, M., & Kay, L. E. 2007, ApJ, 668, L31
Mundell, C. G., Wilson, A. S., Ulvestad, J. S., & Roy, A. L. 2000, ApJ, 529, 816
Mushotzky, R. F., Done, C., & Pounds, K. A. 1993, ARA&A, 31, 717
Nagar, N. M., Wilson, A. S., Mulchaey, J. S., & Gallimore, J. F. 1999, ApJS, 120, 209
Pal, I., Stalin, C. S., Chatterjee, R., & Agrawal, V. K. 2023, JApA, 44, 87
Poutanen, J., & Svensson, R. 1996, ApJ, 470, 249
Poutanen, J., Veledina, A., & Zdziarski, A. A. 2018, A&A, 614, A79
Rees, M. J. 1984, ARA&A, 22, 471
Reeves, J. N., Fabian, A. C., Kataoka, J., et al. 2006, Astron. Nachr., 327, 1079
Rivers, E., Markowitz, A., Rothschild, R., et al. 2014, ApJ, 786, 126
Salpeter, E. E. 1964, ApJ, 140, 796
Shakura, N. I., & Sunyaev, R. A. 1973, A&A, 24, 337
Stern, B. E., Poutanen, J., Svensson, R., Sikora, M., & Begelman, M. C. 1995, ApJ, 449, L13
Strüder, L., Briel, U., Dennerl, K., et al. 2001, A&A, 365, L18
Sunyaev, R. A., & Titarchuk, L. G. 1980, A&A, 86, 121
Tagliacozzo, D., Marinucci, A., Ursini, F., et al. 2023, MNRAS, 525, 4735
Tamborra, F., Matt, G., Bianchi, S., & Dovčiak, M. 2018, A&A, 619, A105
Tanimoto, A., Ueda, Y., Odaka, H., et al. 2020, ApJ, 897, 2
Thorne, K. S., & Price, R. H. 1975, ApJ, 195, L101
Tortosa, A., Bianchi, S., Marinucci, A., Matt, G., & Petrucci, P. O. 2018, A&A, 614, A37
Turner, M. J. L., Abbey, A., Arnaud, M., et al. 2001, A&A, 365, L27
Ursini, F., Petrucci, P. O., Bianchi, S., et al. 2020, A&A, 634, A92
Ursini, F., Matt, G., Bianchi, S., et al. 2021, MNRAS, 510, 3674
Weisskopf, M. C., Soffitta, P., Baldini, L., et al. 2022, J. Astron. Telesc. Instrum. Syst., 8, 026002
Wilkins, D. R., & Fabian, A. C. 2012, MNRAS, 424, 1284
Willingale, R., Starling, R. L. C., Beardmore, A. P., Tanvir, N. R., & O'Brien, P. T. 2013, MNRAS, 431, 394
Wilson, A. S., & Baldwin, J. A. 1985, ApJ, 289, 124
Wilson, A. S., Baldwin, J. A., & Ulvestad, J. S. 1985, ApJ, 291, 627
Yuan, F., & Narayan, R. 2014, ARA&A, 52, 529
Zdziarski, A. A., Johnson, W. N., & Magdziarz, P. 1996, MNRAS, 283, 193
Zdziarski, A. A., Poutanen, J., & Johnson, W. N. 2000, ApJ, 542, 703
Zhang, W., Dovčiak, M., & Bursa, M. 2019, ApJ, 875, 148
Życki, P. T., Done, C., & Smith, D. A. 1999, MNRAS, 309, 561